Earth and Planetary Science Letters 472 (2017) 69–81

Contents lists available at ScienceDirect

Earth and Planetary Science Letters

www.elsevier.com/locate/epsl

Coupled magmatism–erosion in continental arcs: Reconstructing the history of the Cretaceous Peninsular Ranges batholith, southern California through detrital hornblende barometry in forearc sediments

Hehe Jiang*, Cin-Ty A. Lee

Department of Earth Science, Rice University, Houston, TX, United States

ARTICLE INFO

Article history:
Received 18 November 2016
Received in revised form 3 May 2017
Accepted 6 May 2017
Available online xxxx
Editor: A. Yin

Keywords:
Peninsular Ranges
batholith
forearc basin
erosion
detrital hornblende
barometry

ABSTRACT

Continental magmatic arcs are characterized by voluminous flare-ups accompanied by rapid arc unroofing and sedimentation in the forearc basin. Such magmatism and erosion may be dynamically linked and influence the long-term evolution of crustal thickness. To evaluate these effects, we conducted a case study in the Peninsular Ranges batholith (PRB) in southern California, where mid-Late Cretaceous (125–75 Ma) emplacement of felsic plutons coincided with a major pulse of arc-derived sediments into the adjacent forearc basin. We compiled zircon U–Pb ages in the PRB plutons and estimated magmatic addition rates from exposed areas of plutons with different ages. To obtain erosion rates, sandstone samples of known depositional age from the PRB forearc basin were investigated. Major element compositions of detrital hornblendes were determined by electron probe microanalysis and used to calculate emplacement depths of eroded plutons using Al-in-hornblende barometry. These results were combined with laser ablation ICPMS based U–Pb ages of accompanying detrital zircons to estimate the integrated erosion rate by dividing the detrital hornblende emplacement depth by the lag time between peak detrital zircon age and depositional age. Both magmatic addition and erosion rates are between 0.1–2 km/Myr. Magmatic addition peaked at 100–90 Ma, followed by a long, protracted period of erosion between 90–50 Ma. Mass balance and isostatic modeling suggests that due to high magmatic influx, more than 30 km integrated crustal growth and 5 km elevation increase was achieved shortly after peak magmatism. The data and models suggest that erosion was driven by magma-induced crustal thickening and subsequent surface uplift, with an erosional response time of 3–6 Myr. Prolonged erosion after the cessation of magmatism resulted in gradual smoothing of the topography and significant removal of the excess crustal thickness by late Eocene time. The short erosional response times inferred from this study suggest that erosion and magmatism are intimately linked, begging the question of whether the thermal state, metamorphism and rheology of crust in continental arcs is controlled in part by the interplay between erosion and magmatism. We speculate that syn-magmatic erosion, through its effects on the thermal structure of the crust, may also play a role in modulating the depth of pluton emplacement.

1. Introduction

Continental crust is formed in continental arcs through magmatic addition and differentiation, the former derived from partial melting of the mantle or crust and the latter giving rise to the evolved geochemical signatures of continental crust (Kelemen, 1995; Plank, 2005; Lee et al., 2007). Of interest here is how magmatism influences crustal thickness. A thickened/thinned arc crust will have a strong influence on the depth of mantle melting and intracrustal magmatic differentiation as well as development of crustal thermal structure, which suggests there may be dynamic feedbacks between magmatic flux and crustal thickness (Hildreth and Moorbath, 1988; Lee et al., 2007; Chiaradia, 2015; Turner et al., 2016). With thick crust, continental arcs often become high-standing features on Earth and thus may also impact atmospheric circulation and climate (Molnar and England, 1990; Lee et al., 2015).

What controls crustal thickness is the interplay between tectonic forces, magmatic addition and erosion (Karlstrom et al., 2014; Lee et al., 2015; Cao and Paterson, 2016). Both tectonic shortening and influx of mantle-derived magma are processes that thicken the crust, triggering large scale uplift and corresponding erosional processes that thin the crust. Previous studies emphasized the role

* Corresponding author.
E-mail address: hehe.jiang@rice.edu (H. Jiang).

http://dx.doi.org/10.1016/j.epsl.2017.05.009
0012-821X/

of tectonic shortening in crustal thickening (Allmendinger et al., 1997; Haschke and Günther, 2003; Cao and Paterson, 2016). However, continental arcs are characterized by voluminous magmatic flare-ups over tens of millions of years (Ducea, 2001; DeCelles et al., 2009), during which magmatic thickening may be significant. Observations in modern continental arc volcanoes suggest that considerable surface uplift accompanies magmatic input (Fialko and Paearse, 2012; Ward et al., 2014), indicating a large contribution of magmatism to crustal thickening. Close temporal links between high magmatic influx and rapid arc unroofing in ancient arc systems also suggests an important role of magmatism in modulating topography, which in turn controls erosion (Kimbrough et al., 2001). How this dynamic link between magma addition and surface response influences crustal growth in continental arcs is not well understood, mainly because the magnitudes and timing of magmatic and erosional fluxes are not well constrained.

Here, in a case study of forearc sediments derived from a segment of the Cretaceous North American Cordilleran arc, we estimate magmatic addition and erosion rates from established geochronologic data in the arc batholith, along with our own geochronologic and barometric constraints from detrital minerals in forearc sediments. We show from mass balance and isostatic modeling that magmatic thickening was significant during a magmatic flare-up in this arc, and that erosion responded quickly, lagging behind peak magmatism by 3–6 Myr. We propose that this dynamic link between magmatism and erosion dictates the evolution of crustal thickness as well as crustal thermal structure in continental arcs.

2. Peninsular Ranges Batholith and forearc basin

The northern Peninsular Ranges Batholith (PRB) in southern California is one segment of the Cordilleran arc that developed on the western margin of North American continental crust during eastward subduction of the Farallon oceanic plate. The batholith consists of gabbroic to granitic plutons intruded into Paleozoic–Jurassic meta-sedimentary rocks. Emplacement of PRB plutons began in Middle Jurassic time, but most of the batholith was emplaced between 125 and 80 Ma, among which the 100–90 Ma La Posta-type plutons comprise more than 40% of the northern PRB (Kistler et al., 2003; Shaw et al., 2003; Morton et al., 2014; Premo et al., 2014) (Fig. 1). The batholith has been divided into western, eastern, and upper plate zones that are distinct in composition and age (Gastil, 1975; Todd et al., 1988; Kistler et al., 2003; Lee et al., 2007; Morton et al., 2014). The older western zone plutons (125–105 Ma) are gabbroic to tonalitic in composition, and intruded into a prebatholithic basement consisting of Mesozoic island arcs accreted to North America during Late Jurassic–Early Cretaceous extensional subduction (Lee et al., 2007; Morton et al., 2014). Younger eastern zone plutons (105–90 Ma) are predominately granodioritic in composition, and were emplaced through the Paleozoic North American continental margin during a compressional subduction phase (Lee et al., 2007; Morton et al., 2014). The upper plate zone comprises granitic plutons of 92–80 Ma age emplaced into an allochthonous crustal block (Todd et al., 1988; Morton et al., 2014). Eastward younging of the plutons may have been caused by arc front migration due to slab flattening (Grove et al., 2003; Morton et al., 2014) or reduction of the mantle wedge by crustal thickening (Karlstrom et al., 2014). These three zones are separated by two narrow synbatholithic ductile shear zones developed ~118–105 Ma and ~90–80 Ma, respectively (Todd et al., 1988; Morton et al., 2014). Regional scale contraction mostly occurred in the backarc and was complete by 105 Ma (Kimbrough et al., 2001; Grove et al., 2008). Apart from two shear zones, the PRB plutons are undeformed to weakly deformed, indicating that the stress regime in the shallow crust within the arc was neutral to extensional during pluton emplacement (Kimbrough et al., 2001).

Throughout the batholith, Al-in-hornblende thermobarometry of exposed plutons as well as contact metamorphic phase equilibria suggest plutons were emplaced at depths of 10–20 km, with shallower depths recorded in the western part of the batholith (Ague and Brandon, 1992; Todd et al., 2003). The west–east increase in emplacement depths is considered to be a result of Neogene regional uplift associated with rifting of the Gulf of California (Silver and Chappell, 1988; Todd et al., 2003). Thermochronologic studies of the plutons by Grove et al. (2003) and Miggins et al. (2014) suggest progressive cooling from west to east following magmatic emplacement, which they attribute to denudation related to magmatic thickening and/or refrigeration by slab flattening.

Sedimentation in the PRB forearc started as early as early Aptian (122–115 Ma) (Grove et al., 2008). Rapid sedimentation during Cenomanian–Turonian time (100–90 Ma) coincided with emplacement of the La Posta-type plutons. Sequences of forearc strata (2–12 km) developed from the Cenomanian to Eocene in coastal plain and offshore environments along the western flank of the Peninsular Ranges, extending from the northern Santa Ana Mountains to Baja California (Fig. 1) (a summary of the Upper Cretaceous–Lower Eocene PRB forearc strata is included in supplementary material S1). Petrographic studies suggest that the pre-Cenomanian forearc sediments consist mainly of metamorphic and volcanic detritus, representing erosion of old wall rocks and unroofing of the volcanic cover of the arc (Grove et al., 2008). A shift in provenance rock types occurred after the late Cenomanian–Turonian, when detritus from plutonic materials with detrital zircon ages similar to those in the PRB became dominant in the forearc sediments, indicating that by ~90 Ma, the PRB had become a continuous, high-standing topographic feature that isolated the forearc basin from inboard source regions (Nordstrom, 1970; Schoellhamer et al., 1981; Girty, 1987; Sharman et al., 2014). Ages of detrital zircons from forearc sediments deposited during Late Cretaceous–Early Paleogene time suggest that these sediments were derived exclusively from the PRB (Sharman et al., 2014). Unroofing of most of the PRB was largely complete by the end of the Cretaceous. Paleogene stability of the PRB is indicated by >50 Ma apatite fission track ages, preservation of Paleocene–Eocene paleosols, development of Eocene erosional surfaces, and transition from local PRB to extraregional sediment provenance after late Paleocene (Santa Ana Mountains area) – early Eocene time (San Diego area) (Minch, 1979; Abbott, 1981; Miggins et al., 2014; Sharman et al., 2014).

Kimbrough et al. (2001) and Grove et al. (2003) proposed that the close temporal relation between the voluminous magma emplacement of the La Posta suite and the rapid sedimentation initiated in Cenomanian–Turonian indicates strong coupling between high flux magmatic addition and arc exhumation. Lack of large scale contraction throughout the batholith during the magmatic flare-up suggests that the PRB likely represents an example of an arc in which the erosional topography and crustal growth were primarily driven by magmatic thickening (Kimbrough et al., 2001). Understanding how erosion responded to magmatism and the extent to which magmatism and erosion influenced crustal thickness evolution requires quantitative constraints on rates of magmatism and erosion through time.

3. Approaches

3.1. Magmatic addition rates

Magmatic addition rates can be estimated from age distributions and areas of different intrusive suites of the PRB. We com-

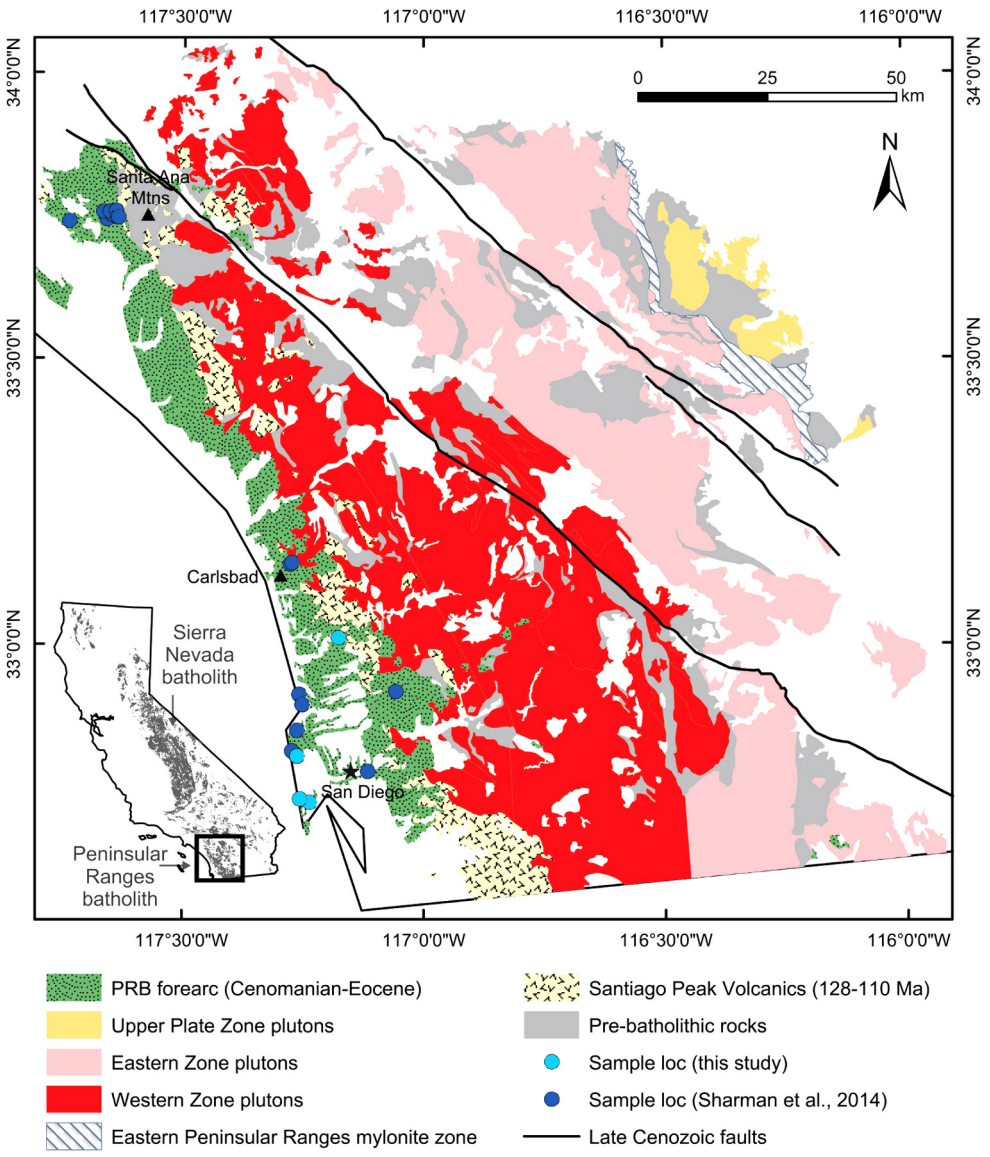

Fig. 1. Geologic map of the northern Peninsular Ranges (modified after Sharman et al. (2014)). The insert map of California show Cretaceous plutonic rocks and location of the Peninsular Ranges batholith, and the main map shows the major units in the PRB and Late Cretaceous–Early Eocene forearc units. Light blue dots are locations of sandstone samples analyzed in this study (lat and long information is in supplementary material S2). Dark blue dots are locations of sandstone samples from Sharman et al. (2014) used in this study. (For interpretation of the references to color in this figure legend, the reader is referred to the web version of this article.)

piled zircon U–Pb ages for PRB plutons from the literature and created age contours at intervals of 10 Myr on a geologic map (Walawender et al., 1990; Thomson and Girty, 1994; Shaw et al., 2003; Premo et al., 2014). Areas of plutons within each 10 Myr interval measured from the map are plotted against plutonic ages in Fig. 2A. Total volume of magmas can be calculated from the areal distribution of the plutons multiplied by the thickness of crust occupied by plutons. This thickness is uncertain due to modification from various crustal processes, such as erosion and delamination. However, bounds can be estimated from current observations on crustal thickness in continental arcs. Seismic studies in the PRB by Barak et al. (2015) suggest that ~15–30 km of current crust is occupied by felsic plutons. Thermobarometric studies by Ague and Brimhall (1988a) and Todd et al. (2003) suggest 10–20 km emplacement depth of the exposed plutons. Therefore, the felsic plutons occupied at least 30 km original crustal thickness. Maximum crustal thickness for the felsic plutons in the PRB is unknown due to erosion and/or delamination, but studies on active continental arcs suggest that the crustal thickness can be up to 60 km (Chiaradia, 2015). Therefore, we use 60 km as a possible maximum bound in calculation of the magmatic volumetric rate. Final magmatic thickening rates or magmatic flux ($km^3/km^2/Myr$) were then obtained by dividing the volumetric addition rate by the total area of the plutons.

3.2. Erosion rates

Because the Upper Cretaceous–Early Paleogene forearc sediments are enriched in plutonic detritus, and are derived exclusively from the PRB, erosion rates after ~90 Myr can be obtained by tracking the emplacement depths of eroded plutons through time (Fig. 3).

We define the lag time (Δt) as the time difference between the stratigraphic age (t_s) of the sediment from which a sample was taken and the sample's igneous age (t_c):

$$\Delta t = t_c - t_s \quad (1)$$

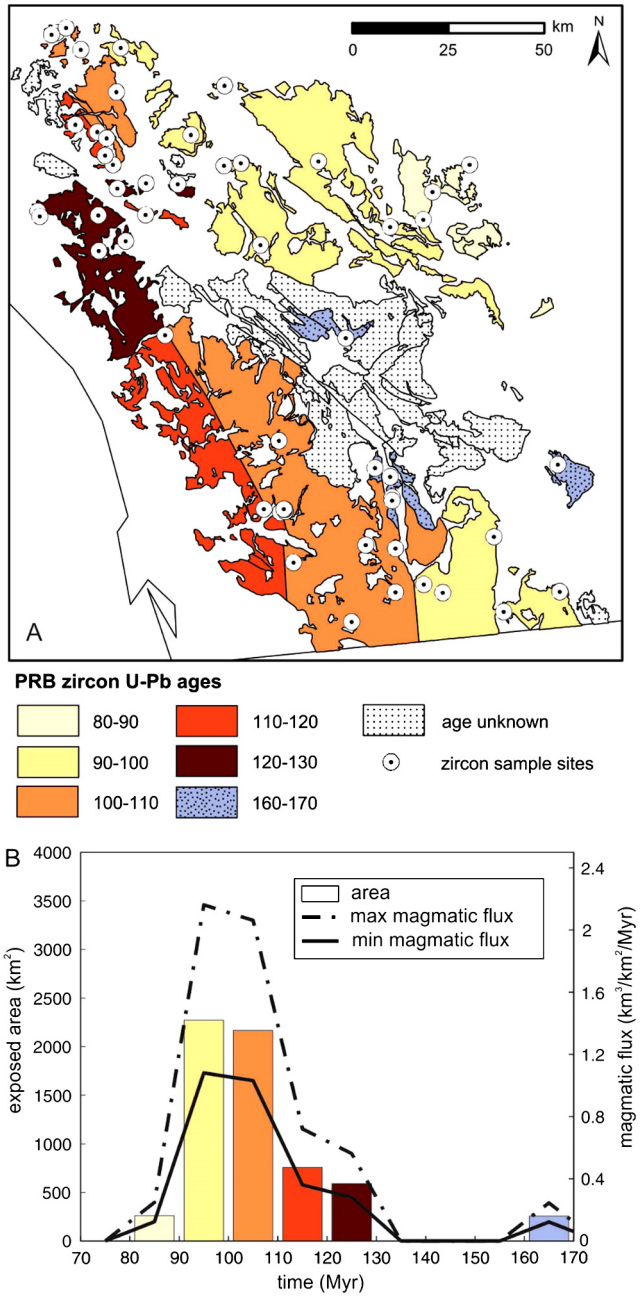

Fig. 2. A) Pluton age map compiled from zircon U–Pb ages. Zircon U–Pb age information is from Walawender et al. (1990), Thomson and Girty (1994), Shaw et al. (2003) and Premo et al. (2014). **B)** surface areas of plutons within each 10 Myr age group and magmatic fluxes. The minimum magmatic flux was calculated assuming the plutons occupy 30 km crustal thickness, and the maximum flux was calculated assuming a 60 km crustal thickness. For details see text in section 3.1.

Given that sediment transport time from source to sink is short in active margin settings (Garver et al., 1999), this lag time represents the time taken for the pluton to be exhumed from its crystallization or emplacement depth (d) to the surface. Similar to magmatic addition rate, the average erosion rate $\overline{E}$ across the batholith since pluton emplacement leading up to the time of deposition of the sample can be calculated as:

$$\overline{E} = \frac{A^{\Delta t}_{eroded} \cdot d}{A_{batholith} \cdot \Delta t} \tag{2}$$

where $A^{\Delta t}_{eroded}$ is the area of batholith being eroded during Δt, and $A_{batholith}$ is the total area of the PRB. The term on the numerator represents the volume of eroded material. $\overline{E}$ has unit of $km^3/km^2/Myr$.

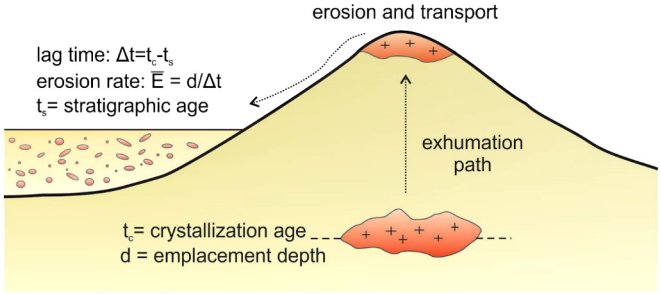

Fig. 3. Schematic diagram showing erosion of a pluton in a continental arc and how erosion rate is calculated. A pluton emplaced at time t_c and emplacement depth d moves toward the surface during arc unroofing. Here we assume erosion is the primary exhumation mechanism. Debris eroded from pluton is transported and deposited at the forearc at time t_s. In active margins where sediment transport time is short, average erosion rates can be approximated by the product between pluton emplacement depth and lag time Δt, which represents the time needed to exhume the pluton to the surface.

It has been suggested that by the Late Cretaceous, erosion of the batholith was well underway, shedding sediments to adjacent forearc and backarc basins (Grove et al., 2003; Sharman et al., 2014). We assume $\frac{A^{\Delta t}_{eroded}}{A_{batholith}} \approx 1$, and average erosion rate can be approximated to:

$$\overline{E} = \frac{d}{\Delta t} \tag{3}$$

In the above equations, t_s is stratigraphic age of a forearc unit, established through previous paleontological and/or paleomagnetic studies (see supplementary material S1 for details and references on strata age constraints). Zircon U–Pb age has been interpreted to represent the pluton crystallization/emplacement age (Coleman et al., 2004; Premo et al., 2014). The Upper Cretaceous–Lower Eocene PRB forearc strata are characterized by nearly unimodal detrital zircon age distributions (Sharman et al., 2014 and this study, details in below sections), therefore t_c can be obtained from the average age of the main peak of the detrital zircon population. The Al-in-hornblende barometer records pressures at or near magma solidification and has been widely applied to determine pluton emplacement pressure/depth in granitic system (Hammarstrom and Zen, 1986; Hollister et al., 1987; Ague and Brimhall, 1988b; Johnson and Rutherford, 1989; Schmidt, 1992; Anderson and Smith, 1995; Todd et al., 2003; Mutch et al., 2016). In the PRB, most plutons contain mineral assemblages that are appropriate for applying Al-in-hornblende barometry (Ague and Brimhall, 1988b; Todd et al., 2003). Therefore, Al content in detrital igneous hornblendes constrains the original emplacement depths of the eroding plutons. We found that the distribution of plutonic emplacement depths recorded in the detritus is unimodal (details in below sections), thus the plutonic emplacement depth d, can be represented by the average "detrital" emplacement depth.

The above approach captures the first-order vertical variation in the crustal thickness through magmatism and erosion across the batholith. Potential uncertainties in the calculated magmatic addition rates and erosion rates include the assumed thickness of crust occupied by felsic plutons and variability in detrital zircon ages and inferred emplacement depths of plutons. The effect of lateral variations in magmatism and erosion, such as eastward migration of magmatism (Todd et al., 1988; Morton et al., 2014) and extension of the forearc drainage area (Sharman et al., 2014) are averaged out by normalizing the volume of magmatic addition/eroded material to the total area of the batholith.

4. Sample description

We collected sandstone samples from Upper Cretaceous–Lower Eocene PRB forearc strata within the Carlsbad–San Diego area (full descriptions of the forearc strata and sample locations are in supplementary material S1 and S2). The oldest sample, from the Lusardi Formation, is a fluvial sandstone deposited directly on plutonic and metamorphic wall-rock of the PRB. Younger sediments were deposited in submarine fans, including the Upper Cretaceous Point Loma Formation and Cabrillo Formation, and the Lower Eocene Mount Soledad Formation. The sandstones consist of angular to subangular and poorly to moderately sorted framework grains with clay matrix or calcite cements. In general, the framework grains are 30–50% quartz, 40–60% feldspar (mostly plagioclase) and up to 10% lithic fragments of various types. Heavy minerals include biotite, amphiboles (mostly hornblende), chlorite, Fe-oxides and zircon. Previous analyses of quartz population and clast composition of coeval conglomerate (e.g. Nordstrom, 1970; Girty, 1987) suggest that the sediments were derived from the exposed plutonic/metamorphic root of a magmatic arc.

5. Analytical methods

Four samples were crushed and panned. Detrital hornblende and zircon grains from each sample were hand-picked from the heavy fraction. These hornblende and zircon grains were then mounted in epoxy and polished. U–Th–Pb isotopes in zircon were analyzed by laser ablation inductively coupled plasma mass spectrometry (LA-ICPMS), and major element concentrations in hornblende were analyzed by Electron Probe Micro-Analysis (EPMA).

5.1. LA-ICPMS for U–Th–Pb isotopes in zircon

U–Th–Pb isotopic data in detrital zircon were collected using a ThermoFinnigan Element 2 magnetic sector mass spectrometer equipped with a New Wave 213 nm laser ablation system at Rice University. The instrument was tuned to achieve sensitivity of 700,000–1,000,000 cps for ^{238}U in zircon standard 91500 (TIMS ^{206}Pb/^{238}U age: 1062.4 ± 0.4 Ma, U concentration ~80 ppm) (Wiedenbeck et al., 1995) with a 30 μm spot size, 10 Hz repetition rate and 9–11 J/cm^2 laser fluence (Jiang et al., 2015). Analyses for the zircon standard and detrital samples were conducted under the same above instrument conditions. Each analysis includes 15–20 s background acquisition followed by ~100 s laser ablation. ^{204}Pb, ^{206}Pb, ^{207}Pb and ^{208}Pb were measured under counting mode, while ^{232}Th and ^{238}U were measured under analog mode. More details in parameter setups for data acquisition were described in Jiang et al. (2015). Each set of 10–20 analyses of unknowns were bracketed by 3–5 analyses of zircon 91500. Paleozoic zircon from Bohemian Massif, Plešovice, Czech Republic (TIMS age: 337.13 ± 0.37 Ma) (Sláma et al., 2008) were also included in each run to monitor accuracy. Due to small grain size of detrital zircons, only one analysis was performed on each grain.

Data reduction was done using an in-house Excel-Visual Basic program (Jiang et al., 2015). For each analysis, average background intensities for Pb isotopes are subtracted from sample intensities. Correction for time-dependent downhole fractionation in ^{206}Pb/^{238}U and ^{208}Pb/^{232}Th in zircon standard 91500 was done by least squares projecting back to the ratios at the initiation of laser ablation. Downhole fractionation for unknowns was corrected by applying the averaged fractionation factors in analyses of zircon 91500 bracketing the unknowns. Due to fractionation of U, Th and Pb during laser ablation, background subtracted and downhole corrected isotopic ratios of the unknowns are corrected by normalizing to the reference value of zircon 91500. Analyses of Plešovice zircon throughout the runs give average value of 338 ± 3 Myr ($n = 62$), consistent with the TIMS age (Sláma et al., 2008).

For each analysis, we calculated the degree of discordance (difference between the ^{207}Pb/^{235}U and ^{206}Pb/^{238}U ages). We also calculated the fraction of common lead (f_{206}) using the ^{207}Pb method described in Williams (1998), assuming a common ^{207}Pb/^{206}Pb ratio of 0.842 ± 0.02 from the Pb evolution model of Stacey and Kramers (1975), which is appropriate for crustal differentiation ages between 0–400 Ma. Analyses with >15% discordance or >1% f_{206} were rejected. Analyses used in construction of age histograms and probability diagrams were corrected for common Pb using the same method by Williams (1998).

Histograms for ^{206}Pb/^{238}U ages for each sample are plotted in Fig. 4. Pb/U, Pb/Th and Pb/Pb ratios for detrital zircon are reported in Supplementary Table 1. Analytical uncertainties for individual analyses are reported at the 68.3% confidence interval (1σ). These uncertainties reflect counting errors in U, Th and Pb measurements. Typical analytical uncertainty of the ^{206}Pb/^{238}U age for the unknown is ~1–2% (1σ). Systematic uncertainties include uncertainties in decay constants for ^{238}U (0.16%) and ^{235}U (0.21%) (Jaffey et al., 1971), uncertainty in the age of standard 91500, average uncertainty in external calibration, and average uncertainty of the common Pb composition. These systematic errors are around 1% (1σ) for ^{206}Pb/^{238}U ages.

5.2. EPMA for major elements in hornblende

Hornblende mounts were carbon coated and analyzed for major element composition on a JEOL JXA8530F Hyperprobe at Rice University, using 4 wavelength-dispersive spectrometers. Analysis was performed using a 15 kV, 20 nA electron beam with 10 μm spot size. For each analysis, counting time is 10 s on peak and 5 s on lower and upper backgrounds, respectively. Natural standards were used for measuring the characteristic X-rays and ZAF matrix correction method was applied for quantification.

Most detrital hornblende grains appear to be homogeneous in optical and backscattered electron images. We did 1–3 analyses on each hornblende grain near the center of the grains. Multiple analyses on a single grain were placed adjacent to each other. These duplicated/triplicated analyses were performed to estimate heterogeneity in composition and monitor biases from effects of surface roughness. Intra-grain variations in Al content are less than 5%. For grains with multiple analyses, we calculated the averages of their chemical compositions, and used the averages in calculation of the Al-in-hornblende barometer and emplacement depths. Weight percentages of major oxides from single spot analyses and averages are reported in supplementary Table 2. Cation abundances were calculated using the method by Leake et al. (1997), assuming 23 oxygen and 13 cations (excluding Ca, Na and K) for each formula.

Prior to calculating pressures and depth, we filtered the data to exclude grains with Fe/(Fe + Mg) outside the range of 0.4–0.65, and/or $Fe^{3+}/(Fe^{3+} + Fe^{2+})$ less than 0.2 (Fe^{3+} and Fe^{2+} were determined from stoichiometric balance using method by Leake et al. (1997)). Such hornblendes are typically found in low fO_2 granites. Compositions of these hornblendes exceed the recommended range for barometry and would yield elevated apparent pressure estimates (Schmidt, 1992; Anderson and Smith, 1995). 0–15% data from each sample were excluded by the $Fe^{3+}/(Fe^{3+} + Fe^{2+})$ and Fe/(Fe + Mg) test.

6. Al-in-hornblende geobarometry in detrital hornblendes

The premises of the Al-in-hornblende geobarometer are that Al content of hornblende is buffered by a nine-phase assemblage (quartz + alkali feldspar + plagioclase + hornblende +

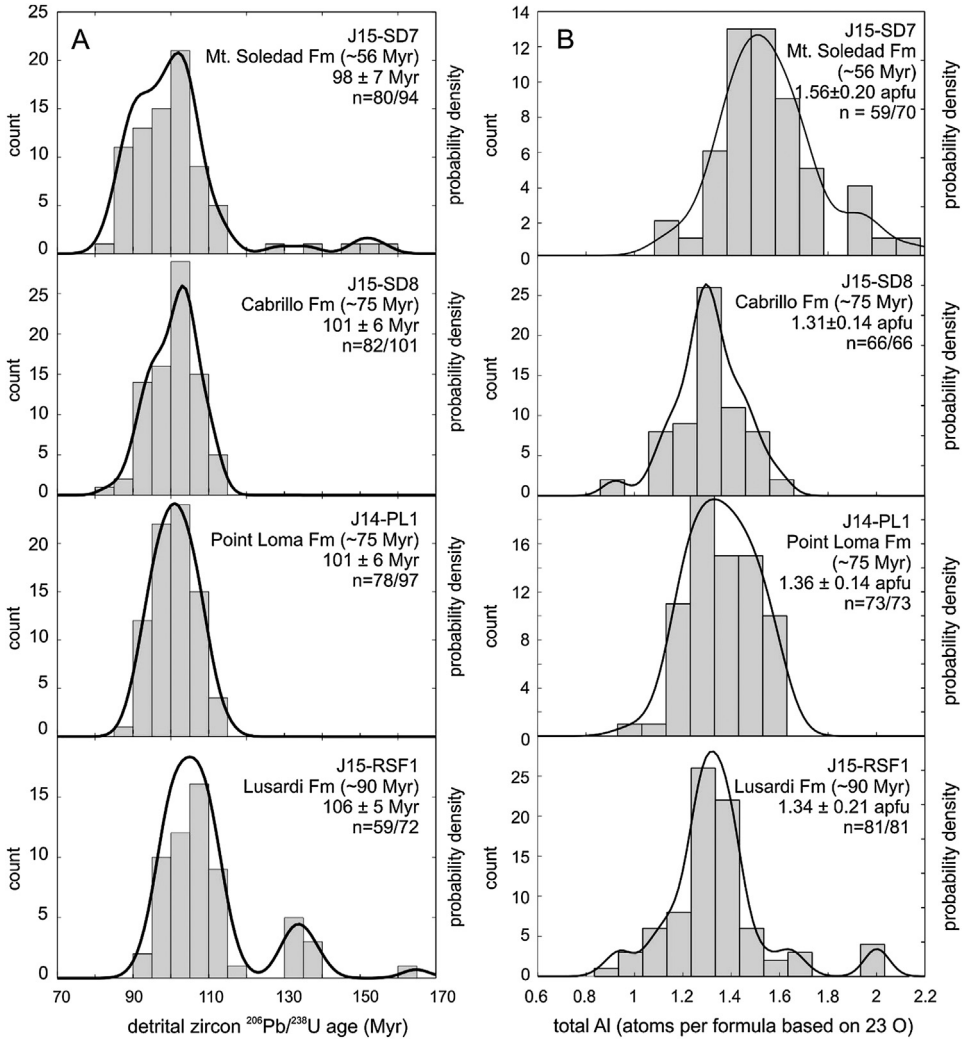

Fig. 4. A) Histograms and kernel density estimates for detrital zircon $^{206}Pb/^{238}U$ ages for sandstone samples from the Upper Cretaceous–Lower Eocene Peninsular Ranges forearc basin. Notice that only zircons with age younger than 170 Myr are displayed here. For full age information, see supplementary table ST1. **B)** Histograms and kernel density estimates for Al content in detrital hornblende from the same samples with detrital zircon ages. Al apfu (atoms per formula unit) is calculated from hornblende major element composition determined by EPMA, normalized to formula with 23 oxygen and 13 cations excluding Ca, K and Na (Leake et al., 1997). Estimated stratigraphic ages, averages and one standard deviations of main peaks and number of detrital grains used in construction of histogram diagram/total number of analyzed grains in each sample are shown on each sub-diagram (details in data filtering strategies are in section 5).

biotite + Fe–Ti oxide + titanite + melt + fluid), and the temperature of hornblende equilibration is near solidus. Once the low-variance phase equilibrium is achieved, Al in hornblende is mainly controlled by the pressure-sensitive tschermakite substitution and temperature-sensitive edenite substitution (Hollister et al., 1987; Johnson and Rutherford, 1989; Schmidt, 1992; Anderson and Smith, 1995) (details in the substitution mechanisms in hornblendes from the PRB plutons and forearc sediments are in supplementary material S3). For igneous rocks, mineral assemblages can be easily identified, and solidus temperature can be obtained from independent geothermometers (e.g. hornblende–plagioclase thermometer, Zr saturation temperature, metamorphic mineral assemblages in the country rocks, etc.). For sedimentary rocks, the biggest challenge of applying Al-in-hornblende geobarometer to detrital hornblendes is that the original contextual relationship between hornblende and other minerals are lost during erosional and sedimentary processes, thus neither equilibrium phase assemblage nor solidus temperature for the parent igneous rocks are clear.

In our case, majority of the PRB plutons consist of the requisite minerals for Al-in-hornblende barometry, which gives a first-order constraint on the original mineral assemblage accompanied with the detrital hornblendes (Ague and Brimhall, 1988b; Todd et al., 2003). Additional constraint can be made from hornblende geochemistry. Previous studies on hornblende stability suggest that SiO_2 saturation of the melt is among the most important factors controlling hornblende geochemistry (Spear, 1981; Hammarstrom and Zen, 1986; Johnson and Rutherford, 1989). Before quartz crystallization, hornblende composition varies with activity of SiO_2. Once quartz begins crystallize, the subsequent hornblende crystallization will not be affected by changes in the bulk SiO_2 content. Hornblendes crystallized from SiO_2-undersaturated system under pressure of 1–8 kbar and temperature of 650–850 °C are characterized by very low A-site occupancy (typically less than 0.1 atoms per formula unit (apfu)) compared with those crystallized from a fully buffered system (SiO_2-saturated, requisite phases are all present, and hornblende are in equilibrium with these phases) under similar pressure and temperature conditions (Spear, 1981).

Detrital hornblendes from the Peninsular Ranges forearc sediments are generally homogeneous in composition, and are characterized by high A site occupancy (supplementary material S3). Compositions of these detrital hornblendes also overlap well with those from PRB igneous rocks with requisite mineral assemblages (Todd et al., 2003), as well as those from Al-in-hornblende

barometer calibration experiments (Johnson and Rutherford, 1989; Schmidt, 1992; Mutch et al., 2016). This suggests that the detrital hornblendes were crystallized in equilibrium with Si-saturated melts and likely fully buffered.

Ideally, application of the Al-in-hornblende barometer requires temperature correction, because solidus of intermediate – felsic melt varies with fluid composition (Anderson and Smith, 1995). Todd et al. (2003) analyzed paired hornblende–plagioclase from a few PRB plutons with requisite mineral assemblage for Al-in-hornblende barometer, and their results suggest 650–800 °C equilibrium temperatures. For each forearc sample with a set of analyses of detrital hornblendes, we therefore applied a Monte-Carlo method by assigning temperature randomly generated within the above temperature range to each analysis. The randomly generated temperatures are either uniformly distributed, or normally distributed with a mean and one standard deviation of 720 ± 40 °C. Within each simulation, we calculated pressures using the empirical calibration of Anderson and Smith (1995), which was developed after experimental calibrations of Johnson and Rutherford (1989) and Schmidt (1992) under conditions between 1–10 kbar and 650–800 °C. We discarded results with pressure <0.5 kbar, which is the low pressure limit for amphibole stability as suggested by Mutch et al. (2016). We repeated the simulation 1000 times, and calculated the mean and standard deviation of pressures from all simulations. Average emplacement depths can then be calculated from pressure estimates assuming a 2.75 g/cm^3 density for felsic crustal rocks (Rudnick and Fountain, 1995) (Fig. 5).

The approach we lay out above gives a general guideline of application of Al-in-hornblende geobarometry in detrital hornblendes. Because successful application of this barometer requires that hornblende is equilibrated in a low-variance system, consideration on the original mineral assemblage, composition of detrital hornblende, as well as possible solidus range must be made prior to pressure calculation. It is noticeable that the Monte-Carlo simulation introduces large uncertainties in the calculated pressure (section 7.3). It is likely that for any specific hornblende, some of the randomly sampled temperatures may not be within the range of the true solidus of the melt in equilibrium with the hornblende, or certain phase may be absent at these temperatures, which will result in overestimated/underestimated pressure. However, this approach takes full consideration of temperature effect on Al-in-hornblende pressure when conventional geothermometry is not applicable. It also gives the maximum possible range of pressure recorded in the detritus population. Apparent pressures calculated using other calibrations made within fixed temperatures or without temperature corrections will show narrower range, but all fall within that of the Monte-Carlo simulations (supplementary material S4).

7. Results

7.1. Constraints on magmatic addition rates

Magmatic fluxes estimated from the exposed pluton area assuming the magmas occupied between 30 to 60 km crustal thickness are shown in Fig. 2B. Magmatic flux commences at 130 Myr, peaks at 1.1–2.2 km/Myr at ~95 Myr, decreases rapidly at 95–85 Myr, and terminates after 80 Myr. Because we considered the crust as bounded by the Moho, any mafic cumulates, such as pyroxenites (Lee et al., 2007), are not accounted for in our magmatic flux estimates. Thus, our magmatic flux estimates only account for the contribution from the felsic component of the total magmatic flux. In considering elevation, it is the felsic component that is most important due to its low density.

7.2. Detrital zircon ages

Detrital zircons from all strata have U–Pb ages that predominantly fall within the zircon age range in PRB plutons. All zircons from sample J14-PL1 and J15-SD8 have ages within 120–80 Ma. In sample J15-RSF1 and J15-SD7, up to 15% of the detrital zircons are from older PRB rocks (170–130 Myr) and 2% are from Precambrian–Paleozoic wall rocks (Fig. 4A and supplementary table ST1). The main peak age shifts slightly from 106 Ma to 98 Ma from Cretaceous to Eocene forearc strata. Overall the distribution of the zircon ages is consistent with the duration of the main magmatic pulse in the PRB. The shift in peak age is likely caused by the eastward migration of watershed catchments within the batholith that fed the forearc basin, as suggested by Sharman et al. (2014).

7.3. Detrital Al-in-hornblende pressures and emplacement depths

In the Upper Cretaceous samples, Al concentrations in the detrital hornblendes are similar, ranging from 0.8–1.8 atoms per formula unit (apfu) on a 23 oxygen basis, peaking at 1.3–1.4 apfu (Fig. 4B). Al in hornblende is higher in the Lower Eocene sample, ranging from 0.9–2.3 apfu and peaking at 1.5 apfu. Previous Al-in-hornblende barometric studies of the PRB plutons suggest 1–1.5 apfu Al in the western PRB and 1.25–2 apfu Al in the eastern PRB, while most plutons have Al within the range of 1.25–1.75 apfu (Ague and Brimhall, 1988b; Todd et al., 2003) (supplementary material S5). Similarity in Al content in hornblende from detritus and plutons suggests that the eroded plutons were likely emplaced under similar temperature and pressure conditions with plutons *in situ*.

In our Monte-Carlo simulation calculation, regardless of the type of distribution of input temperatures, the calculated pressures from all samples are near normally distributed (Fig. 5). For each sample, pressures calculated using different temperature distributions give similar means and standard deviations. This unimodal distribution of calculated pressures in the forearc detrital hornblendes indicates that the eroded plutons were emplaced at a preferential depth range. The three Upper Cretaceous samples yield $2.5–2.7 \pm 1$ kbar pluton emplacement pressure, corresponding to pluton depth of $\sim 10 \pm 4$ km. The Lower Eocene sample yields pressure of $\sim 3.7 \pm 1.2$ kbar and emplacement depth of $\sim 13.5 \pm 4$ km. This pressure/depth range overlaps well with that recorded from the PRB plutons (2–5 kbar, 7–18 km) (Todd et al., 2003) (supplementary material S5). It is therefore reasonable to assume that 10–13.5 km represents the characteristic average depth of pluton emplacement in the PRB.

7.4. Erosion rates

We calculated time-integrated erosion rates for each horizon using equations (1) and (3) (Fig. 6, Table 1). The uncertainty in erosion rate was propagated using the standard deviation of the main peak of the detrital zircon age (~±5 Myr) and detrital emplacement depth distributions (±4 km), and estimated uncertainty in the depositional age (±3–5 Myr). We also estimated erosion rates in samples using data from Sharman et al. (2014), which were collected from a broader region than this study (including the northern Santa Ana Mountains and San Miguel Island). We chose only those which have PRB zircon signals. Sharman et al. (2014) report detrital zircon ages, but no data on detrital hornblende compositions; for these samples, we assumed a 10 ± 4 km pluton emplacement depth for those deposited during the Late Cretaceous and 13.5 ± 4 km for those deposited during Paleocene–Eocene.

Despite large uncertainties, the calculated average erosion rates are within the same order of magnitude of the magmatic rates

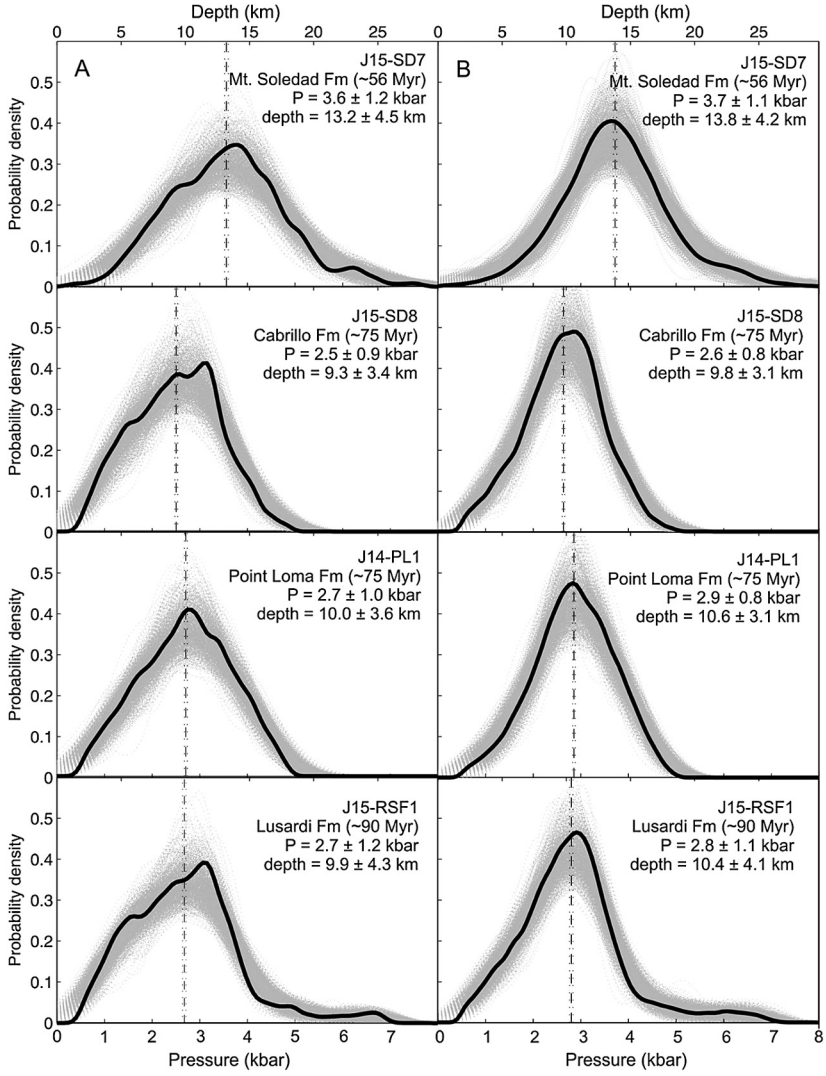

Fig. 5. Emplacement depths calculated from detrital hornblende Al content through Monte-Carlo approach with input temperatures either in uniform distribution (A) or normal distribution (B) (details in section 6). Light gray thin curves are kernel density estimates of each simulation, and thick black curves are kernel density estimates of all simulations. Averages and one standard deviation of pressures and depths were calculated from the distribution of all simulations.

and show a decreasing trend since 90 Ma (Fig. 6). Overall, erosion rates calculated in this study agree with those derived from thermochronological data in the PRB through thermal modeling from previous studies (Lovera et al., 1999; Grove et al., 2003) and sediment accumulation rates in the southern PRB forearc (Kimbrough et al., 2001). The decreasing trend in the erosion rates in general follows the decline in magmatic flux after the 100–90 Ma magmatic peak, but erosion continues well beyond the cessation of magmatism.

8. Discussion

8.1. Erosional response time and crustal thickness evolution

The effect of the coupling of magmatism and erosion on crustal growth can be expressed by a simple mass balance equation in which crustal thickness is controlled through magmatic thickening and erosional thinning (Lee et al., 2015):

$$\frac{dH}{dt} = \dot{M} - \dot{E} \tag{4}$$

where H is crustal thickness (km), t is time (Myr), $\dot{M}$ is magmatic addition rate (km/Myr) and $\dot{E}$ is erosional rate (km/Myr). Elevation (h) is related to isostatic adjustment to changes in crustal thickness:

$$\frac{dh}{dH} = 1 - \frac{\rho_c}{\rho_m} \tag{5}$$

where ρ_c and ρ_m are densities of crust (2.75 g/cm^3) and mantle (3.3 g/cm^3), respectively. Erosion is driven by elevation change, which can be expressed by equation:

$$\dot{E} = \frac{h}{\tau_E} \tag{6}$$

where τ_E is the erosion response time, which describes how long it will take to erode a given elevation h and represents the efficiency of erosion (Simoes et al., 2010). Since isostatic equilibrium can be achieved within a few thousands of years after perturbation (Cathles, 1975), which is negligible compared to the life span of continental arc magmatism, τ_E also represents the time for erosion in response to the elevation change induced by arc magmatism. τ_E is inversely proportional to precipitation rate (p, m/yr) and substrate erodibility (k_e, m^{-1}) by $\tau_E = (p \cdot k_e)^{-1}$ (Simoes et al., 2010), and is estimated to be 1.75–14 Myr in modern mountain belts (Lee et al., 2015). Eqs. (4)–(6) show that magmatism drives erosion, that is, magmatic addition into the crust triggers surface uplift, which

Table 1
Stratigraphic ages, main peak ages in detrital zircon U–Pb age distributions for samples in this study (denoted by "*") and from Sharman et al. (2014), and calculated lag time and erosion rates. Sources for stratigraphic ages are in supplementary material S1. Erosion rates in the Sharman et al. (2014) samples were calculated assuming 10 ± 4 km pluton emplacement depth for Upper Cretaceous samples, and 13.5 ± 4 km emplacement depth for Cenozoic samples. Estimated uncertainties are included (see text in section 7.4 for details). Unit is Myr for ages and km/Myr for erosion rates.

Sample	Formation	Main peak age (t_c)	t_c 1σ	Stratigraphic age (t_s)	t_d 1σ	Lag time (Δt)	Δt 1σ	Erosion rate (E)	E 1σ
San Diego									
J15-RSF1*	Lusardi	106	4.9	90	5	16	7.1	0.63	0.37
ROSA-5	Lusardi	109	4.6	90	5	19	6.8	0.53	0.28
ROSA-4	Lusardi	111	4.7	90	5	21	6.9	0.48	0.25
J14-PL1*	Point Loma	101	6.0	75	3	26	6.7	0.38	0.18
ROSA-3	Point Loma	100	5.7	75	3	25	6.4	0.40	0.19
J15-SD8*	Cabrillo	102	7.1	72	3	29	7.7	0.40	0.13
ROSA-1	Cabrillo	99	5.5	72	3	27	6.2	0.37	0.17
J15-SD7*	Mount Soledad	98	7.3	56	3	42	7.9	0.31	0.11
JOLLA-3	Mount Soledad	110	3.8	56	3	60	4.8	0.25	0.08
JOLLA-4	Mount Soledad	109	5.9	56	3	59	6.6	0.25	0.08
Santa Ana Mountain									
TRB	Trabuco	106.9	4.0	93	5	13.9	6.4	0.72	0.44
BAK	Baker Cyn.	103.8	3.5	90	5	13.8	6.1	0.72	0.43
MUST	Holz Shale	100	6.5	78	3	22	7.2	0.45	0.22
WLM	Williams	98	4.6	74.5	3	23.5	5.5	0.43	0.20
SLVL	Silverado (Lower)	99	6.1	60	3	39	6.8	0.35	0.12
San Miguel Island									
SMI0401	Mirounga	103	6.8	90	5	13	7.5	0.77	0.59
SMI0402	Mirounga	105	7.4	86	3	19	8.0	0.53	0.31
SMI0403	Mirounga	102	6.5	80	3	22	7.2	0.45	0.23
SMI0404	Mirounga	98	7.1	70	3	28	7.8	0.36	0.17

results in the gravitational potential for erosion. Combining equations (4) to (6) yields:

$$\frac{dH}{dt} = \dot{M} - \frac{1}{\tau_E}\left(1 - \frac{\rho_c}{\rho_m}\right)H \tag{7}$$

which shows that crustal thickness is primarily controlled by magmatic thickening $\dot{M}$ and modulated by the kinetics of erosion, as represented by the inverse of the erosional response time τ_E. For short τ_E (efficient erosion kinetics), erosion catches up quickly with magmatic thickening, resulting in near steady state crustal thickness and topography, wherein crustal thickening by magmatism is balanced by erosion. For longer τ_E, erosion significantly lags behind magmatism, resulting in development of a thick crust and protracted erosional decrease in topography tens of million years after magmatism (Fig. 6).

We modeled evolution of crustal thickness, elevation and erosion using Eqs. (4) through (6) and magmatic fluxes calculated from section 3.1 with different τ_E values, assuming 30 km initial (pre-magmatic) crustal thickness and 0 km initial elevation (Fig. 6). To compare the model with the erosion rates inferred from detrital barometry in the previous section, we also calculated time-averaged erosion rate $\overline{E}$ from the modeled instantaneous erosion rate $\dot{E}$ as the time-integrated erosional extent divided by the lag time:

$$\overline{E} = \frac{\int_{t_s}^{t_c} \dot{E} dt}{\Delta t} \tag{8}$$

Since detrital zircons from most samples have peak ages around 100 Myr, we used $t_c = 100$ Myr in Eq. (8) to model the integrated erosion rates.

We note that cumulative erosion in the model continues to increase with time, exceeding the Al-in-hornblende pressures. The simplest explanation for this difference is that the barometric pressures represent pluton emplacement depths and that crustal thickness approached steady state, wherein erosion rates have caught up with the magmatic flux. We will return to this concept later, but what this observation implies is that the emplacement depths recorded in the sediments, particularly the younger sediments, are minimum bounds on the total erosion extent prior to deposition. This means that erosion rates inferred from the sediments, particularly in the younger strata, should be lower than the modeled average erosion rate, but higher than the instantaneous erosion rate. In older strata, which are close in age to the plutons, our sediment-inferred erosion rates should approximate instantaneous erosion rates but should be higher than the modeled average erosion rate.

With the above concepts in mind, we can place bounds on the erosional response time by comparing the modeled average and instantaneous erosion rates for different response times and magmatic fluxes with erosion rates determined from detrital hornblende barometry. In Fig. 7, we calculate the maximum erosion rates as well as the time span over which erosion rate decreases from its maximum to ~1/e of the maximum (the "e-fold time") from the model. The modeled e-fold time is independent of the magnitude of magmatic flux, but with the same response time, instantaneous erosion rate decreases faster than the average erosion rate. The e-fold time for the estimated erosion rates is ~40 Myr, which should lie between that of the modeled instantaneous rate and time-averaged rate (Fig. 7A). In Fig. 7B the two sets of curves calculated using the lower and upper bound of magmatic fluxes bracket the range of maximum erosion rates that can be reached with different erosional response times. The maximum erosion rate inferred from detrital barometry (0.75 km/Myr) then gives an additional constraint on the erosional response time.

These constraints on e-fold time and maximum erosion rate give a τ_E range of 3–6 Myr. For these response times, our models indicate 10–30 km of excess crustal growth and 5 km elevation rise within 40 Myr after initiation of magmatism, with peak crustal thickness and elevation being established shortly after 90 Myr (Fig. 6C, G). Our models indicate that most of this excess crustal thickness and elevation would have been removed by Late Eocene time. Indeed, thermochronologic studies on the PRB and detrital zircon studies on the forearc suggest slow exhumation of the

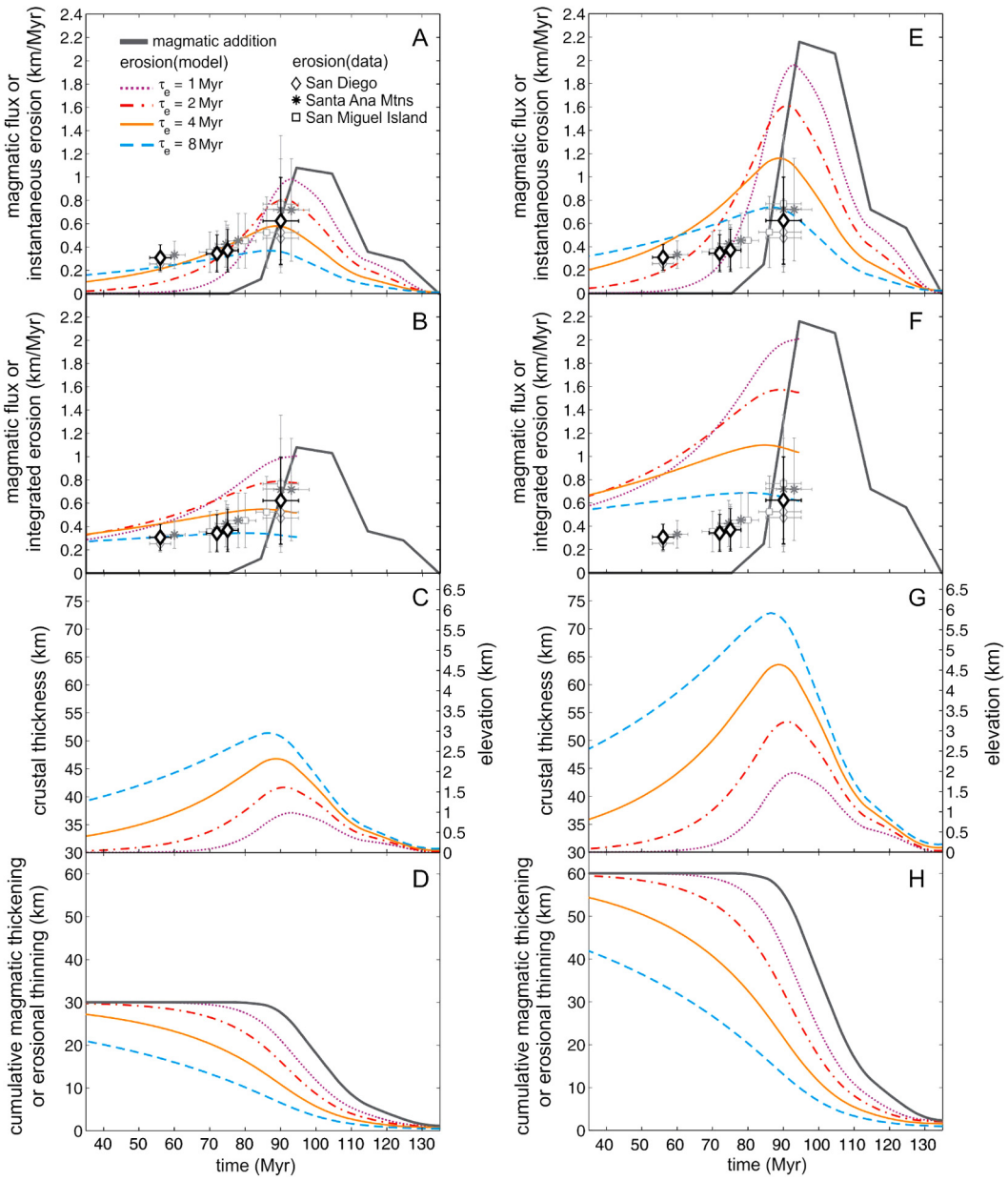

Fig. 6. Mass balance and isostatic model results for average and instantaneous erosion rates, excess crustal thickness, and elevation. Also shown are cumulative magmatic thickening and erosional thinning calculated using the minimum (A–D) and maximum (E–H) magmatic fluxes from Fig. 2 for erosional response times of 1, 2, 4, and 8 Myr. Erosion rates calculated from detrital zircon age and detrital hornblende barometry are superimposed on Figs. 6A, B, E and F. Samples analyzed in this study are highlighted with thick symbols. Samples from Sharman et al. (2014) are in thin light gray symbols. Error bars in erosion rates and depositional age are in 1σ.

batholith and eastward migration of sedimentary sources (Miggins et al., 2014; Sharman et al., 2014), suggesting crustal thickness and elevation had decreased by that time. This peneplenation of the PRB to low elevations by late Eocene time is also suggested by Minch (1979) and Sharman et al. (2014). The current high elevations of the PRB could be the result of recent tectonism and hot and buoyant asthenospheric mantle associated with opening of the Gulf of California and are not relevant here (Lewis et al., 2000).

8.2. On the thickness of continental arcs

Our models predict that, even with significant syn-magmatic erosion, the arc crust will thicken considerably. Crustal thickness during magmatism should scale with the magmatic flux, modulated by the efficiency of erosion. Consistent with our models is the observation of high La/Yb and Sr/Y ratios in the eastern PRB, which reflects garnet fractionation during magmatic differentiation and implies crustal thickness exceeded 40 km during Late Cretaceous magmatism (Gromet and Silver, 1987; Lee et al., 2007). One question, however, is whether crustal thickening is controlled mainly by tectonic shortening or magmatism. Previous structural studies in the central Andes and Sierra Nevada suggest that the relative contribution of crustal thickening by tectonic shortening versus magmatic addition is 2:1 (Haschke and Günther, 2003; Cao and Paterson, 2016). The amount of tectonic thickening in the PRB is not clear, but if this 2:1 ratio also applies to the PRB, the total thickening rate would have to be three times our estimated magmatic addition rate. To achieve the 0–1 km/Myr erosion rates over 40 Myr after peak magmatism, erosional response times would have to be three times our estimated value, or extension would have to take place to compensate for the crustal thickening. However, there is little evidence for significant syn- and post-magmatism extension in the PRB. With such high thickening

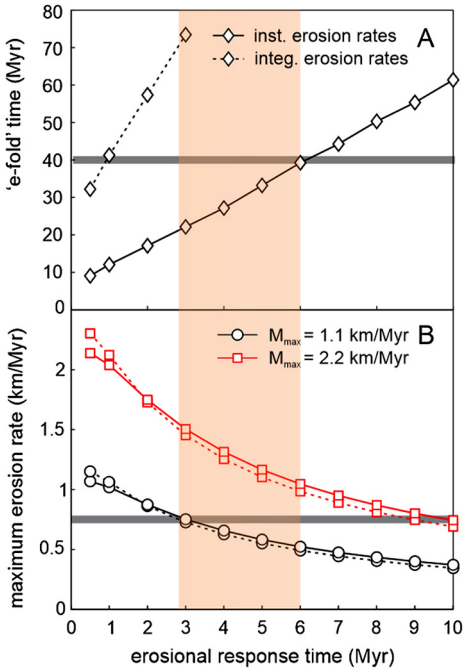

Fig. 7. Constraints on erosional response time from the e-fold time (duration for erosion rate decreasing from its maximum to 1/e of the maximum) (A) and maximum erosion rate (B). Thin lines with symbols are calculated from the model (Eqs. (4)–(8)). Solid lines are for instantaneous erosion rates, and dashed lines are for time-averaged erosion rates. Thick horizontal gray lines are constraints inferred from stratigraphic age and detrital zircon and hornblende data. The highlighted area shows the overlap between ranges in erosional response time constrained from the e-fold time and maximum erosion rate, respectively.

rates and a 3-fold response time, crustal thickness of over 100 km would be predicted, which would seem to be unrealistically high. In addition, the long response time needed to accommodate over 100 km crustal thickness does not appear to agree with the observation of the near synchronicity of peak magmatism and rapid erosion. Therefore, there may not be significant tectonic thickening in the PRB. Because other parts of the Cretaceous Cordillera arc appear to have similar arc–forearc evolution history and tectonic conditions (DeGraaff-Surpless et al., 2002; DeCelles et al., 2009; Gehrels et al., 2009), this coupled magmatism–erosion process may be prevalent throughout the arc and play a more important role than previously considered in controlling crustal thickness and topography.

Seismic studies suggest a ~30 km crustal thickness of the eastern PRB (Lewis et al., 2000; Barak et al., 2015), which is less than the syn-magmatic crustal thickness. This difference in crustal thicknesses indicates that considerable crustal material was removed after magmatism ceased. Proposed mechanisms for the evolution of PRB crustal thickness have included magmatic addition, tectonic shortening, exhumation, delamination, subduction erosion, gravity-driven collapse and extension (Thomson and Girty, 1994; Lee et al., 2007; Grove et al., 2008). Our work suggests that some of this thinning could have been controlled by post-magmatic erosion.

8.3. Pluton emplacement depths and the role of erosion

One surprising finding in this study is the similarity of Al content in detrital hornblendes, corresponding to similar emplacement depths of 10–15 km, from sediments of different ages as well as from the exposed plutons. One would expect shallower plutons to be eroded first, progressively reaching deeper level plutons with more exhumation. This apparent dilemma can be reconciled if erosion and magmatism are nearly in phase. Al-in-hornblende

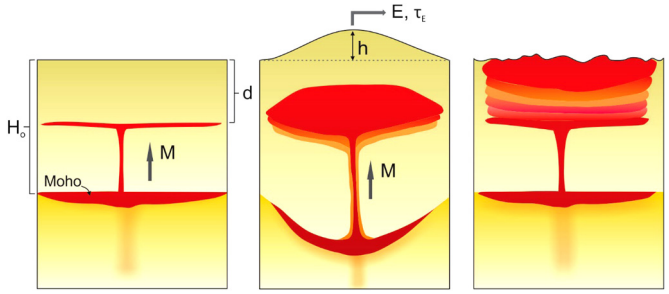

Fig. 8. Schematic diagram showing coupled magmatism–erosion in continental arcs. Large influx of magma in the arc led to magmatic thickening, uplift and erosion, which brings old plutons to the surface and provide "space" for newly added magma. With a short erosional response, erosion catches up with magmatism. As a result, plutons with different age record similar emplacement pressure at the mid-crust.

pressures record magma emplacement depths, which imply then that magmas tend to be emplaced, at any given time, at similar depths rather than randomly throughout the crustal column. If erosion responds quickly to magmatic addition, one can approach a steady state scenario in which magmas are emplaced in the mid-crust, forcing older and solidified plutons to be exhumed. At steady state, all plutonic material will therefore record similar emplacement pressures (Fig. 8). The regional uniformity of Al-in-hornblende pressures in other batholiths, along with the similar 10–20 km mid-crustal emplacement depths (Ague and Brimhall, 1988b; Chadwick et al., 2000; Tulloch and Challis, 2000; Todd et al., 2003; Hervé et al., 2007; Needy et al., 2009), suggests that plutons are emplaced at a characteristic depth and that magmatism is distinctly tied to erosion. Exactly what controls the depth of emplacement is unclear, but quantities such as stress state, rheology of the crust and magma, thermal state, and buoyancy likely all play a role regionally. Regardless, tight coupling of magmatism and erosion requires that the cumulative amount of erosion in any given magmatic belt will likely be much larger than that inferred from emplacement pressures. Estimates of magmatic flux, based on observed crustal thicknesses, are thus minimum bounds if the magmatic orogen has approached steady state. Coupling of erosion with magmatism may also provide a simple solution to the long-standing "room problem" for pluton emplacement (Petford et al., 2000; Burov et al., 2003). Erosion facilitates pluton emplacement into the crust by providing accommodation (e.g. through roof-lifting) for intrusion.

8.4. Implications for crustal thermal structure

The coupling of magmatism and erosion could strongly influence the thermal and mechanical structure of the crust, generating complex feedbacks between pluton emplacement and erosion. Although magmatic advection is the dominant mechanism of heat transport in active continental arcs (Rothstein and Manning, 2003), rapid erosion can also exhume rocks from depth, the resulting heat advection will cause an elevated geothermal gradient in the upper crust. In combination, magma addition and erosion act together to heat up the crust (Fig. 9A). Such heating will promote higher temperature regional metamorphism. Recent studies by Chu and Ague (2015) have shown that classic Barrovian metamorphic sequences actually show a component of very high temperature metamorphism in terranes with magmatic pulses. Elevation of the geotherm will also alter the rheology of the crust with time, decreasing the effective strength and viscosity of the crust, which in turn would decrease resistance to tectonic shortening (Fig. 9B). We might also expect the brittle–ductile transition to shallow with time.

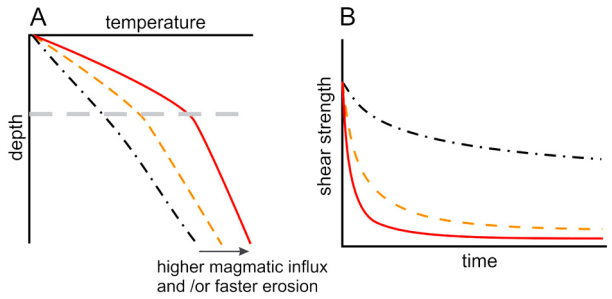

Fig. 9. Schematic effect of coupled magmatism–erosion on geothermal gradient and crustal rheology. **A)** Both magmatism and erosion will strongly advect heat to the surface, resulting in an elevated geothermal gradient. Higher magmatic and/or erosion rates will lead to hotter crust at shallower depths. **B)** Crustal strength, if temperature dependent, changes with time at a given depth (indicated by the thick gray dashed line in A).

9. Conclusions

Using available geochronologic and thermobarometric data from the Cretaceous Peninsular Ranges batholith and its associated forearc basin, we affirm the strong coupling between high flux magmatic addition and rapid unroofing of a continental arc. We show that a magmatic flare-up in the arc can result in significant crustal thickening, triggering uplift and driving long-term erosion. This coupled magmatic thickening and erosional thinning can account for tens of kilometers of variation in crustal thickness on timescales of tens of millions of years and may indirectly influence mantle melting and other arc processes such as delamination and arc front migration (Karlstrom et al., 2014; Chin et al., 2015; Turner et al., 2016). Rapid erosion coupled to magmatism may also play an important role in controlling pluton emplacement depth as well as inducing strong upward advection of heat, resulting in focused heating in the middle-crust and increased geothermal gradients in the mid-upper crust. This change in crustal thermal structure may affect regional metamorphism and lead to weakening of the upper crust. Finally, our study shows that any understanding of how juvenile continental crust is formed requires an understanding of the destructive power of erosion, which is coupled to the processes of generating juvenile crust. The coupled effects of erosion and magmatism should also play an important role in the compositional evolution of the continental crust (Lee et al., 2008) and the effects of magmatic orogens on long term climate change (Lee et al., 2013; Lee and Lackey, 2015).

Acknowledgements

This work was supported by an NSF grant to study the role of continental arcs in long term climate evolution to Lee (OCE-1338842). We thank Gelu Costin for assistance in EPMA analyses, Lexi Malouta for field assistance during sample collection in southern California in 2015, Wenrong Cao for discussions on modeling, and Rajdeep Dasgupta for advice on Al-in-hornblende geobarometry. We thank Glenn Sharman and Andrew Barth for constructive reviews.

Appendix A. Supplementary material

Supplementary material related to this article can be found online at http://dx.doi.org/10.1016/j.epsl.2017.05.009.

References

Abbott, P.L., 1981. Cenozoic paleosols San Diego area, California. Catena 8 (1), 223–237.

Ague, J.J., Brandon, M.T., 1992. Tilt and northward offset of Cordilleran batholiths resolved using igneous barometry. Nature 360, 146–149.

Ague, J.J., Brimhall, G.H., 1988a. Magmatic arc asymmetry and distribution of anomalous plutonic belts in the batholiths of California: effects of assimilation, crustal thickness, and depth of crystallization. Geol. Soc. Am. Bull. 100, 912–927.

Ague, J.J., Brimhall, G.H., 1988b. Regional variations in bulk chemistry, mineralogy, and the compositions of mafic and accessory minerals in the batholiths of California. Geol. Soc. Am. Bull. 100, 891–911.

Allmendinger, R.W., Jordan, T.E., Kay, S.M., Isacks, B.L., 1997. The evolution of the Altiplano–Puna Plateau of the central Andes. Annu. Rev. Earth Planet. Sci. 25 (1), 139–174.

Anderson, J.L., Smith, D.R., 1995. The effects of temperature and fO_2 on the Al-in-hornblende barometer. Am. Mineral. 80, 549–559.

Barak, S., Klemperer, S.L., Lawrence, J.F., 2015. San Andreas Fault dip, Peninsular Ranges mafic lower crust and partial melt in the Salton Trough, Southern California, from ambient-noise tomography. Geochem. Geophys. Geosyst. 16 (11), 3946–3972.

Burov, E., Jaupart, C., Guillou-Frottier, L., 2003. Ascent and emplacement of buoyant magma bodies in brittle–ductile upper crust. J. Geophys. Res., Solid Earth 108 (B4), 2177.

Cao, W., Paterson, S., 2016. A mass balance and isostasy model: exploring the interplay between magmatism, deformation, and surface erosion in continental arcs using central Sierra Nevada as a case study. Geochem. Geophys. Geosyst., 2194–2212.

Cathles, L.M., 1975. Viscosity of the Earth's Mantle. Princeton University Press.

Chadwick, B., Vasudev, V.N., Hegde, G.V., 2000. The Dharwar craton, southern India, interpreted as the result of Late Archaean oblique convergence. Precambrian Res. 99 (1–2), 91–111.

Chiaradia, M., 2015. Crustal thickness control on Sr/Y signatures of recent arc magmas: an Earth scale perspective. Sci. Rep. 5, 1–5.

Chin, E.J., Lee, C.T.A., Blichert-Toft, J., 2015. Growth of upper plate lithosphere controls tempo of arc magmatism: constraints from Al-diffusion kinetics and coupled Lu–Hf and Sm–Nd chronology. Geochem. Perspect. Lett. 1 (0), 20–32.

Chu, X., Ague, J.J., 2015. Analysis of experimental data on divalent cation diffusion kinetics in aluminosilicate garnets with application to timescales of peak Barrovian metamorphism, Scotland. Contrib. Mineral. Petrol. 170 (2), 25.

Coleman, D.S., Gray, W., Glazner, A.F., 2004. Rethinking the emplacement and evolution of zoned plutons: geochronologic evidence for incremental assembly of the Tuolumne Intrusive Suite, California. Geology 32 (5), 433–436.

DeCelles, P.G., Ducea, M.N., Kapp, P., Zandt, G., 2009. Cyclicity in Cordilleran orogenic systems. Nat. Geosci. 2 (4), 251–257.

DeGraaff-Surpless, K., Graham, S.A., Wooden, J.L., McWilliams, M.O., 2002. Detrital zircon provenance analysis of the Great Valley Group, California: evolution of an arc–forearc system. Geol. Soc. Am. Bull. 114 (12), 1564–1580.

Ducea, M., 2001. The California arc: thick granitic batholiths, eclogitic residues, lithospheric-scale thrusting, and magmatic flare-ups. GSA Today 11 (11), 4–10.

Fialko, Y., Paearse, J., 2012. Sombrero uplift above the Altiplano–Puna magma body: evidence of a ballooning mid-crustal diapir. Science 338, 250–252.

Garver, J.I., Brandon, M.T., Roden-Tice, M., Kamp, P.J.J., 1999. Exhumation history of orogenic highlands determined by detrital fission-track thermochronology. Geol. Soc. (Lond.) Spec. Publ., vol. 154, pp. 283–304.

Gastil, R.G., 1975. Plutonic zones in the Peninsular Ranges of southern California and northern Baja California. Geology 3, 361–363.

Gehrels, G.E., et al., 2009. U–Th–Pb geochronology of the Coast Mountains batholith in north-coastal British Columbia: constraints on age and tectonic evolution. Geol. Soc. Am. Bull. 121 (9/10), 1341–1361.

Girty, G.H., 1987. Sandstone provenance, Point Loma Formation, San Diego, California: evidence for uplift of the Peninsular Ranges during the Laramide Orogeny. J. Sediment. Petrol. 57 (5), 839–844.

Gromet, P., Silver, L.T., 1987. REE variations across the Peninsular Ranges batholith: implications for batholithic petrogenesis and crustal growth in magmatic arcs. J. Petrol. 28 (1), 75–125.

Grove, M., Lovera, O., Harrison, M., 2003. Late Cretaceous cooling of the east-central Peninsular Ranges batholith (33°N): relationship to La Posta pluton emplacement, Laramide shallow subduction, and forarc sedimentation. In: Johnson, S.E., et al. (Eds.), Tectonic Evolution of Nortwestern Mexico and the Southwestern USA. In: Geological Society of America Special Paper, vol. 374, Boulder, Colorado, pp. 355–397.

Grove, M., et al., 2008. The Catalina Schist: evidence for middle Cretaceous subduction erosion of southwestern North America. In: Draut, A.E., Clift, P.D., Scholl, D.W. (Eds.), Formation and Applications of the Sedimentary Record in Arc Collision Zones. In: Geological Society of America Special Paper, vol. 436, pp. 355–361.

Hammarstrom, J.M., Zen, E.-A., 1986. Aluminum in hornblende: an empirical igneous geobarometer. Am. Mineral. 71, 1297–1313.

Haschke, M., Günther, A., 2003. Balancing crustal thickening in arcs by tectonic vs. magmatic means. Geology 31 (11), 933–936.

Hervé, F., Pankhurst, R.J., Fanning, C.M., Calderón, M., Yaxley, G.M., 2007. The South Patagonian batholith: 150 my of granite magmatism on a plate margin. Lithos 97 (3–4), 373–394.

Hildreth, W., Moorbath, S., 1988. Crustal contributions to arc magmatism in the Andes of Central Chile. Contrib. Mineral. Petrol. 98 (4), 455–489.
Hollister, L.S., Grissom, G.C., Peters, E.K., Stowell, H.H., Sisson, V.B., 1987. Confirmation of the empirical correlation of Al in hornblende with pressure of solidification of calc-alkaline plutons. Am. Mineral. 72, 231–239.
Jaffey, A.H., Flynn, K.F., Glendenin, L.E., Bentley, W.C., Essling, A.M., 1971. Precision measurement of half-lives and specific activities of ^{235}U and ^{238}U. Phys. Rev. C, Nucl. Phys. 4 (5), 1889–1906.
Jiang, H., Lee, C.-T.A., Morgan, J.K., Ross, C.H., 2015. Geochemistry and thermodynamics of an earthquake: a case study of pseudotachylites within mylonitic granitoid. Earth Planet. Sci. Lett. 430, 235–248.
Johnson, M.C., Rutherford, M.J., 1989. Experimental calibration of the aluminum-in-hornblende geobarometer with application to Long Valley caldera (California) volcanic rocks. Geology 17 (9), 837–841.
Karlstrom, L., Lee, C.T.A., Manga, M., 2014. The role of magmatically driven lithospheric thickening on arc front migration. Geochem. Geophys. Geosyst. 15 (6), 2655–2675.
Kelemen, P.B., 1995. Genesis of high Mg# andesites and the continental crust. Contrib. Mineral. Petrol. 120 (1), 1–19.
Kimbrough, D.L., et al., 2001. Forearc-basin sedimentary response to rapid Late Cretaceous batholith emplacement in the Peninsular Ranges of southern and Baja California. Geology 29 (6), 491–494.
Kistler, R.W., Wooden, J.L., Morton, D.M., 2003. Isotopes and Ages in the Northern Peninsular Ranges Batholith, Southern California. U.S. Geological Survey Open-File Report, 03-489: 45 p.
Leake, B.E., et al., 1997. Nomenclature of amphiboles: report of the subcommittee on amphiboles of the international mineralogical association, commission on new minerals and mineral names. Can. Mineral. 35, 49–76.
Lee, C.T.A., Lackey, J.S., 2015. Global continental arc flare-ups and their relation to long-term greenhouse conditions. Elements 11, 125–130.
Lee, C.-T.A., Morton, D.M., Kistler, R.W., Baird, A.K., 2007. Petrology and tectonics of Phanerozoic continent formation: from island arcs to accretion and continental arc magmatism. Earth Planet. Sci. Lett. 263, 370–387.
Lee, C.-T.A., et al., 2008. Regulating continent growth and composition by chemical weathering. Proc. Natl. Acad. Sci. USA 105 (13), 4981–4986.
Lee, C.-T.A., et al., 2013. Continental arc–island arc fluctuations, growth of crustal carbonates, and long-term climate change. Geosphere 9 (1), 1–16.
Lee, C.-T.A., Thurner, S., Paterson, S.R., Cao, W., 2015. The rise and fall of continental arcs: interplays between magmatism, uplift, weathering, and climate. Earth Planet. Sci. Lett. 425, 105–119.
Lewis, J.L., Day, S.M., Magistrale, H., 2000. Regional crustal thickness variations of the Peninsular Ranges, southern California. Geology 28 (4), 303–306.
Lovera, O.M., Grove, M., Kimbrogh, D.L., Abbott, P.L., 1999. A method for evaluating basement exhumation histories from closure age distributions of detrital minerals. J. Geophys. Res. 104 (B12), 29419–29438.
Miggins, D.P., et al., 2014. Thermochronology of Cretaceous batholitic rocks in the northern Peninsular Ranges batholith, southern California: implications for the Late Cretaceous tectonic evolution of southern California. In: Morton, D.M., Miller, F.K. (Eds.), Peninsular Ranges Batholith, Baja California and Southern California, pp. 199–261.
Minch, J.A., 1979. The Late Mesozoic–Early Tertiary framework of continental sedimentation, northern Peninsular Ranges, Baja California, Mexico. In: Eocene Depositional Systems. San Diego, pp. 43–68.
Molnar, P., England, P., 1990. Late Cenozoic uplift of mountain ranges and global climate change: chicken or egg? Nature 346 (6279), 29–34.
Morton, D.M., et al., 2014. Framework and petrogenesis of the northern Peninsular Ranges batholith, southern California. Mem. Geol. Soc. Amer. 211, 61–143.
Mutch, E.J.F., Blundy, J.D., Tattitch, B.C., Cooper, F.J., Brooker, R.A., 2016. An experimental study of amphibole stability in low-pressure granitic magmas and a revised Al-in-hornblende geobarometer. Contrib. Mineral. Petrol. 171 (10), 85.
Needy, S.K., et al., 2009. Mesozoic magmatism in an upper- to middle-crustal section through the Cordilleran continental margin arc, eastern Transverse Ranges, California. Geological Society of America Special Paper 456, 187–218.
Nordstrom, C.E., 1970. Lusardi Formation: a post-batholithic Cretaceous conglomerate north of San Diego, California. Geol. Soc. Am. Bull. 81, 601–606.
Petford, N., Cruden, A.R., McCaffrey, K.J.W., Vigneresse, J.L., 2000. Granite magma formation, transport and emplacement in the Earth's crust. Nature 408 (6813), 669–673.
Plank, T., 2005. Constraints from Thorium/Lanthanum on sediment recycling at subduction zones and the evolution of the continents. J. Petrol. 46 (5), 921–944.
Premo, W.R., Morton, D.M., Wooden, J.L., Fanning, C.M., 2014. U–Pb zircon geochronology of plutonism in the northern Peninsular Ranges batholith, southern California: implications for the Late Cretaceous tectonic evolution of southern California. In: Morton, D.M., Miller, F.K. (Eds.), Peninsular Ranges Batholith, Baja California and Southern California. In: Geological Society of America Memoir, vol. 211, pp. 145–180.
Rothstein, D.A., Manning, C.E., 2003. Geothermal gradients in continental magmatic arcs; constraints from the eastern Peninsular Ranges Batholith, Baja California, Mexico. Geological Society of America Special Paper 374, 337–354.
Rudnick, R.L., Fountain, D.M., 1995. Nature and composition of the continental crust: a lower crustal perspective. Rev. Geophys. 33 (3), 267–309.
Schmidt, M.W., 1992. Amphibole composition in tonalite as a function of pressure: an experimental calibration of the Al-in-hornblende barometer. Contrib. Mineral. Petrol. 110, 304–310.
Schoellhamer, J.E., Vedder, J.G., Yerkes, R.F., Kinney, D.M., 1981. Geology of the Northern Santa Ana Mountains, California. U.S. Geological Survey Professional Paper, 420-D: 109 p.
Sharman, G.R., Graham, S.A., Grove, M., Kimbrogh, D.L., Wright, J.E., 2014. Detrital zircon provenance of the Late Cretaceous–Eocene California forearc: influence of Laramide low-angle subduction on sediment dispersal and paleogeography. Geol. Soc. Am. Bull..
Shaw, H.R., Todd, V.R., Grove, M., 2003. Jurassic peraluminous gneissic granites in the axial zone of the Peninsular Ranges, southern California. In: Johnson, S.E., et al. (Eds.), Tectonic Evolution of Northwestern Mexico and the Southwestern USA. In: Geological Society of America Special Paper, vol. 374, pp. 157–183.
Silver, L.T., Chappell, B.W., 1988. The Peninsular Ranges Batholith: an insight into the evolution of the Cordilleran batholiths of southwestern North America. Trans. R. Soc. Edinb. Earth Sci. 79, 105–121.
Simoes, M., Braun, J., Bonnet, S., 2010. Continental-scale erosion and transport laws: a new approach to quantitatively investigate macroscale landscapes and associated sediment fluxes over the geological past. Geochem. Geophys. Geosyst. 11 (9), 1–22.
Sláma, J., et al., 2008. Plešovice zircon — a new natural reference material for U–Pb and Hf isotopic microanalysis. Chem. Geol. 249 (1–2), 1–35.
Spear, F.S., 1981. An experimental study of hornblende stability and compositional variability in amphibolite. Am. J. Sci. 281, 697–734.
Stacey, J.S., Kramers, J.D., 1975. Approximation of terrestrial lead isotope evolution by a two-stage model. Earth Planet. Sci. Lett. 26, 207–221.
Thomson, C.N., Girty, G.H., 1994. Early Cretaceous intra-arc ductile strain in Triassic–Jurassic and Cretaceous continental margin arc rocks, Peninsular Ranges, California. Tectonics 13 (5), 1108–1119.
Todd, V.R., Erskine, B.G., Morton, D.M., 1988. Metamorphic and tectonic evolution of the northern Peninsular Ranges batholith, southern California. In: Ernst, W.G. (Ed.), Metamorphism and Crustal Evolution of the Western United States (Rubey Volume 7), pp. 894–937.
Todd, V.R., Shaw, S.E., Hammarstrom, J.M., 2003. Cretaceous plutons of the Peninsular Ranges batholith, San Diego and westernmost Imperial Counties, California: Intrusion across a Late Jurassic continental margin. In: Johnson, S.E., et al. (Eds.), Tectonic Evolution of Northwestern Mexico and the Southwestern USA. In: Geological Society of America Special Paper, vol. 374, Boulder, Colorado, pp. 185–235.
Tulloch, A.J., Challis, G.A., 2000. Emplacement depths of Paleozoic–Mesozoic plutons from western New Zealand estimated by hornblende-Al geobarometry. N.Z. J. Geol. Geophys. 43, 555–567.
Turner, S.J., Langmuir, C.H., Katz, R.F., Dungan, M.A., Escrig, S., 2016. Parental arc magma compositions dominantly controlled by mantle-wedge thermal structure. Nat. Geosci. 9 (10), 772–776.
Walawender, M.J., et al., 1990. Origin and evolution of the zoned La Posta-type plutons, eastern Peninsular Ranges batholith, southern and Baja California. In: Anderson, J.L. (Ed.), The Nature and Origin of Cordilleran Magmatism. In: Geological Society of America Memoir, vol. 174, Boulder, Colorado, pp. 1–18.
Ward, K.M., Zandt, G., Beck, S.L., Christensen, D.H., McFarlin, H., 2014. Seismic imaging of the magmatic underpinnings beneath the Altiplano–Puna volcanic complex from the joint inversion of surface wave dispersion and receiver functions. Earth Planet. Sci. Lett. 404, 43–53.
Wiedenbeck, M., et al., 1995. Three natural zircon standards for U–Th–Pb, Lu–Hf, trace element and REE analyses. Geostand. Newsl. 19 (1), 1–23.
Williams, I.S., 1998. U–Th–Pb geochronology by ion microprobe. In: McKibben, M.A., Shanks III, W.C., Ridley, W.I. (Eds.), Applications of Microanalytical Techniques to Understanding Mineralizing Processes. In: Reviews in Economic Geology, pp. 1–35.